UNIVERSITÉ
DE GENÈVE

Report for the Astrophysics Lab II
submitted June 30, 2022

Red supergiants mass loss:

Investigating a new mass loss prescription with the Geneva stellar evolution code

Joris Josiek,

under the supervision of Sylvia Ekström

ABSTRACT

Stars with an initial mass above 8 solar masses will spend most of their post-main-sequence life as a red supergiant (RSG). This evolutionary phase is characterized by low surface temperature, low surface gravity and very intense radiation, which leads to very heavy mass loss in the form of stellar winds. Mass loss is a dynamical process that cannot be physically implemented in stellar evolution codes, so we rely on empirical prescriptions to calculate the mass loss as a simple function of a few stellar parameters. Beasor *et al.* (2020) established a new RSG mass loss prescription based on observations of stellar clusters. In this work, we investigate the effects of this new mass loss on the evolution of massive stars using the Geneva Stellar Evolution Code (GENEC) and compare the results with previous prescriptions. In particular, we conclude that the new prescription leads to considerably lower mass loss than older models, which explains much better the observation of RSGs at luminosities above $\log(L/L_\odot) > 5.25$.

Contents

Chapter 1

Introduction

1.1 Motivation

Look at a star tonight and again in fifty years, you will probably observe more or less the same thing. Look at it again in a billion years, and it may have changed size, changed color or even completely disappeared. Stars evolve on very long timescales, far longer than the entire history of the modern human, thus making it impossible for us to observe stellar evolution directly.

Fortunately, we now have the technological means to use computational models to help us study the life of a star. This essentially involves feeding all the underlying physics to a computer along with an initial structure of a star and letting the computer press fast-forward on the star's evolution. In addition to letting us watch the whole life of a star in the span of a few minutes, this also has the convenient side-effect that it allows us to learn about the interior of stars.

Alas, there is also considerable difficulty here, which makes this an active field of research. As it turns out, most of the physics involved in stellar evolution is either incredibly complex (even for a computer) or just plainly not yet understood. Either way, we are forced to make many simplifying approximations and assumptions that can compromise the accuracy of our results. Nevertheless, current state-of-the-art simulations are already very good at explaining a plethora of observations and give us a very good idea of the main courses of stellar evolution. The focus now lies in the details, the goal of research being to improve, expand, and test specific physical ingredients of the simulations.

In this work, I investigate mass loss as one ingredient of stellar modeling, specifically looking at mass loss during the late evolutionary stage of massive stars known as the red supergiant (RSG) phase.

1.2 The evolution of massive stars

I shall start by giving a brief summary of the important aspects in the evolution of massive stars. The content of this section is often the subject of an introductory course in stellar astronomy and can be reviewed in standard textbooks such as Maeder (2009).

We consider massive a star that has an initial mass of at least $8\,M_\odot$, a threshold that will separate the late-stage evolution and ultimate fate of a star into two qualitatively different paths. Initially, a star forms from a collapsing gas cloud that heats up as it converts gravitational potential energy into thermal energy. When the core of the young star reaches sufficiently high temperature and density, it begins to fuse hydrogen into helium. This process releases nuclear energy, counteracting gravitational collapse and keeping the star stable for most its life. This phase of stable central hydrogen burning is known as the main sequence (MS) and at the moment of hydrogen ignition, the star is said to be at the zero-age main sequence (ZAMS).

When the hydrogen in the core is depleted, central fusion stops and the stellar core

loses its pressure support. As a result, it begins to contract under its own gravity, heat up and increase its luminosity. This generates radiation pressure that causes the stellar envelope to expand and cool to a red color. It is at this stage that the further evolution of the star bifurcates based on its initial mass. Massive stars become what is known as a red supergiant (RSG), which is the evolutionary phase that we will focus on in this work. It is characterized by a very large radius hundreds of times larger than the sun's, a low surface temperature of a few thousand K, and low surface gravity on the order of 0.1% of the gravity on the Earth's surface.

When the core of a massive star has used up all of its hydrogen, the heat generated by the subsequent contraction is sufficient to ignite helium burning. The helium in the core is fused to carbon via the triple-alpha process (also producing oxygen as a side-effect), while hydrogen fusion continues in a shell around the core. After the helium in the core of a massive star is depleted, the core will contract again and begin fusing carbon to neon, sodium and magnesium, while helium and hydrogen will continue burning in shells around the core. In this fashion, a massive star can fuse successively heavier elements in the core, while continuing to burn the lighter elements in shells.

The timescale between the initiation of each central fusion phase gets successively shorter by orders of magnitude: while central hydrogen burning lasts for on the order of 10 million years for massive stars, central helium burning will cease only 1 million years after its ignition, and central carbon burning after only one thousand years. After central carbon burning, the star only has a few years left to live, during which it still goes through multiple central burning phases.

At the end of its life, the star has built up a shell structure with an outer hydrogen envelope, and inner burning zones of hydrogen, helium, carbon, oxygen, neon, magnesium, and silicon, from outside to inside. The last phase of nuclear fusion – silicon burning – lasts only a few weeks and produces an iron-nickel core, which cannot be used for further fusion to generate energy. Eventually, the inert core collapses under its own gravity, generating a powerful shock wave that causes a violent explosion of the star known as a supernova. Most of the star's material is thus expelled into the interstellar medium to be used for the formation of a new generation of stars. Depending on the mass of the remaining core, it is either crushed into a neutron star or a black hole. Very massive stars are also thought to be able to collapse directly into a black hole without generating a supernova (Smartt 2009).

1.3 The Hertzsprung-Russell diagram

Visualization is a powerful tool that can help us understand the happenings in a star in more detail, and it is therefore appropriate to dedicate some words to this. There are several ways to represent the evolution of a star graphically in order to visually highlight various aspects involved.

A very widespread type of diagram is the Hertzsprung-Russell diagram (HRD), which is a two-dimensional plot showing the a star's luminosity against its surface temperature. Luminosity is a star's radiative power, and surface temperature, also referred to interchangeably as the effective temperature, is defined as the temperature of a black body with the same size and radiative output as the star (Rouan 2011). Note that in an HRD the temperature axis is typically inverted: its cool end is on the right. Since luminosity and surface temperature are two observable quantities, the HRD can be used to classify phases of stellar evolution observationally as well as describe the evolution of a single simulated star, and thus it serves as an interface between observation an theory.

An important stellar parameter that can be directly inferred from the HRD is its radius R. This is done via the Stefan-Boltzmann relation which relates effective temperature to radiative flux.

$$L = 4\pi R^2 \sigma T_{\mathrm{eff}}^4 \tag{1.1}$$

To discuss the use of the HRD in the context of stellar evolution theory, the model tracks for three initial masses are shown in Figure 1.1. I have specifically chosen these three

models out of simulations done in this study because they exemplify the different paths of post-main sequence evolution a massive star can take. The stellar models begin on the ZAMS, which in this mass range can be approximated on the HRD by a power law between luminosity and effective temperature. All three stars become cooler and more luminous after leaving the main sequence as central helium burning begins and the star moves towards becoming a red supergiant. The data extraction tool used to analyze the simulation data flags a star as a red supergiant if its surface temperature T_{eff} and luminosity L satisfy the following conditions.

$$\log(T_{\mathrm{eff}}\ [\mathrm{K}]) \leq 3.66 \qquad \log(L/L_{\odot}) \geq 4 \tag{1.2}$$

Note that this is not a universal criterion defining a red supergiant, and using only HRD position to separate red supergiants from other giant stars such as AGB stars is in fact no trivial task (Neugent *et al.* 2020).

After reaching the RSG phase, a star can either remain there for the rest of its life (e.g. $20\,M_{\odot}$), depart during central helium burning for a short phase of contraction known as a "blue loop" and then return to the RSG phase (e.g. $12\,M_{\odot}$), or depart completely from the RSG phase because of too much mass loss and become a yellow or blue supergiant and die as such (e.g. $30\,M_{\odot}$). It is part of this work to investigate the conditions for any particular HRD track with regards to mass loss.

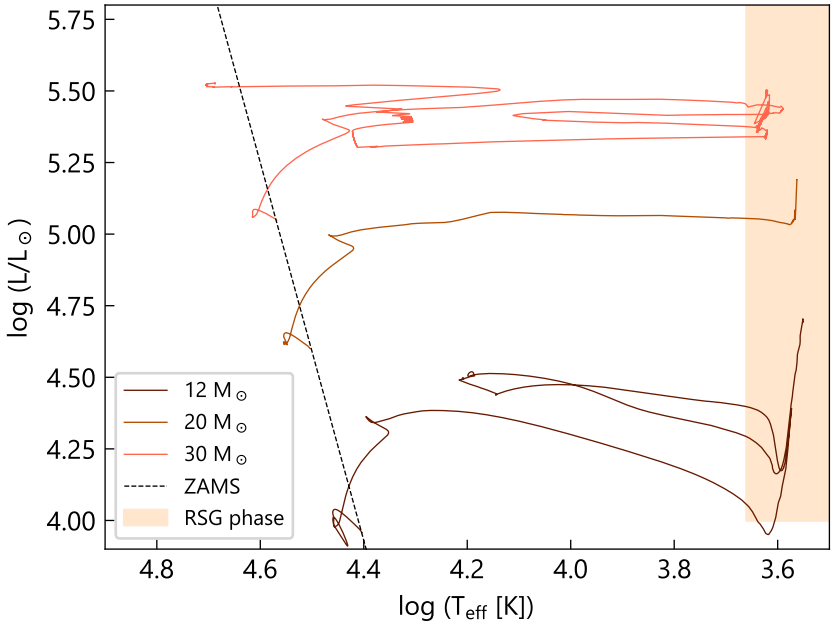

Figure 1.1: Hertzsprung-Russell diagram (HRD) showing the evolution of stellar models from the zero-age main sequence (ZAMS) at three different initial masses. The data is produced by simulations with the Geneva stellar evolution code (GENEC) given the initial conditions of solar metallicity and zero rotation. The standard mass loss prescription was used in the red supergiant phase (See section 1.4).

1.4 Mass loss prescriptions

Throughout their lives, stars eject mass from their surface in the form of stellar winds. Stellar mass loss is most significant when surface gravity is low and radiation is very intense, as is the case during the RSG phase. The physical processes driving mass ejection from a star involve complicated turbulent processes, making numerical treatment of these processes

extremely complex. Implementing mass loss into a stellar evolution code from first principles would require a full three-dimensional treatment of hydrodynamic interactions, which includes tracking the flow of particles and the forces acting on them at each point in the star. This is computationally unrealistic, so we need to find some easier way to treat mass loss.

The solution to this problem has been to compute the stellar mass loss rate as a simple function of accessible stellar parameters, usually at least its luminosity (de Jager *et al.* 1988). A suitable function is an empirical approximation adjusted to fit observations of mass loss, and when implemented in stellar evolution code, it is known as a mass loss *prescription*. It tells the program how much mass the star loses after each time step but has no actual physical basis. As a result, the outcome of the evolution model must be rigorously tested against observations in order to validate such a prescription. As part of this work, I discuss some possible observational constraints as a way of evaluating the validity of the simulations.

Several mass loss prescriptions are being used in stellar evolution codes, each one appropriate under different conditions. Looking at mass loss in the RSG phase, the main prescription being used by the Geneva stellar evolution code is the following one based on a figure in Crowther (2001) using observations by Sylvester *et al.* (1998) and van Loon *et al.* (1999).

$$\log\left(\dot{M}/(M_{\odot}\mathrm{yr}^{-1})\right) = 1.7\log\left(L/L_{\odot}\right) - 13.83 \tag{1.3}$$

One weakness of this prescription is that observations on field stars show a large dispersion of mass loss rates in RSGs of similar luminosities (Beasor & Davies 2016). Observations of RSGs in Galactic clusters, where all stars all have similar metallicities, ages and initial masses, have shown a tight correlation between mass loss rate and luminosity (Beasor & Davies 2016; 2018), suggesting that one or more of the aforementioned parameters are the cause of the dispersion of mass loss rates. Beasor *et al.* (2020) used infrared photometry coupled with modeling of radiative transfer in dust to measure the mass loss rate of red supergiants in Galactic clusters at solar metallicity. They detemined the age of the clusters from their turn-off point in the HRD and used it to constrain the mass of the RSGs in each cluster. They were then able to derive the following new mass loss prescription for RSGs that depends on both luminosity and initial mass.

$$\log\left(\dot{M}/(M_{\odot}\mathrm{yr}^{-1})\right) = -26.4 - 0.3\log\left(M_{\mathrm{ini}}/M_{\odot}\right) + 4.8\log\left(L/L_{\odot}\right) \tag{1.4}$$

1.5 Project Overview

In this project, I run simulations in order to investigate the new RSG mass loss prescription presented in Equation 1.4 and compare its effects on stellar evolution to the standard prescription in Equation 1.3 used previously.

Specifically, I use the GENeva stellar Evolution Code (GENEC) to compute stellar models of initial masses ranging from $12\,M_{\odot}$ to $32\,M_{\odot}$ in increments of $2\,M_{\odot}$ for each of the two mass loss prescriptions, totaling 22 models. All stars shall have solar metallicity and be non-rotating. Furthermore, I shall run the computations only until the end of central carbon burning, because at this point the star has lived 99.99999% of its life and the modeling of advanced phases is computationally expensive. A star cannot undergo significant mass loss in the short time that remains until core collapse.

In chapter 2, I explain the main methods used to compute a stellar model. This includes an brief overview of GENEC and its numerical process as well as a description of the workflow for producing a simulation. I also include a section dedicated to discussing the different possibilities to help the code to convergence in case of difficulties, which is relevant especially for the more massive, unstable stars.

In chapter 3, I present data extracted from the models to highlight the various effects of the different RSG mass loss prescriptions on the evolution of massive stars. In particular, I show evolution tracks on the HRD, discuss timescales for the RSG phase, establish a mass-luminosity relation for RSG stars, and present the evolution of chemical surface abundances.

In chapter 4, I draw conclusions on the results of the study and discuss its validity, observability and limitations within the broader context of massive star evolution.

Chapter 2

Methods

2.1 The Geneva Stellar Evolution Code

The Geneva stellar evolution code (GENEC), presented by Eggenberger *et al.* (2008), is an algorithm written in Fortran 90 used to simulate the evolution of stars from an initial ZAMS model. In this section I will briefly describe how this algorithm works. See Ekström (2021) for a review on stellar modeling, specifically with regards to massive stars.

We must simplify the complex physics of stars into a form that can be computed numerically in an appropriate amount of time. We therefore consider a star to be described by one-dimensional functions depending only on the radial coordinate. Since we are considering non-rotating stars, this spherical symmetry is a good approximation, but of course there are processes such as turbulence and convection that are difficult to treat using only one spatial axis. The radial structure of a star is described by the four following equations, aptly named the equations of stellar structure. They relate the 5 quantities radial mass M_r, mass density ρ, pressure P, temperature T, and luminosity L to the independent radial coordinate r.

Mass continuity:

$$\frac{\mathrm{d}M_r}{\mathrm{d}r} = 4\pi r^2 \rho \tag{2.1}$$

Hydrostatic equilibrium: (G is the graviational constant.)

$$\frac{\mathrm{d}P}{\mathrm{d}r} = -\rho \frac{GM_r}{r^2} \tag{2.2}$$

Energy conservation: (ℓ is the local luminosity, i.e. the net energy transfer per unit time at a specific radius, ϵ is the net nuclear energy production rate density, ϵ_{grav} is the energy production rate density from gravitational energy.)

$$\frac{\mathrm{d}\ell}{\mathrm{d}r} = 4\pi r^2 \rho (\epsilon + \epsilon_{\mathrm{grav}}) \tag{2.3}$$

Radiative transfer: (κ is the opacity, σ is the Stefan-Boltzmann constant.)

$$\frac{dT}{dr} = -\frac{3\kappa\rho}{16\sigma T^3} \frac{\ell}{4\pi r^2} \tag{2.4}$$

These equations are valid under the condition that there is local thermodynamic equilibrium (LTE) as well as hydrostatic equilibrium, i.e. the star is in a stable state and does not evolve dynamically (only quasistatically). The opacity κ and nuclear energy production rate ϵ are functions of density, temperature and chemical composition that can be extracted from tables.

The system of equations is closed by appending an equation of state $P(\rho, T, X_i)$ relating the pressure to density, temperature and chemical abundances. For an ideal gas, the equation of state is as follows.

$$P = \frac{\rho k T}{\mu m_u} \tag{2.5}$$

We have a system of coupled linear differential equations, which we supplement with some boundary conditions.

1. The surface values of the radial mass M_r, luminosity ℓ, and radius r are the corresponding macroscopic stellar parameters: its mass M, luminosity L, and radius R, respectively. These three values are a priori independent, but the next point explains the reduction of the degrees of freedom down to only one, which we typically choose to be the stellar mass M.
2. The radius r and radial mass M_r are zero at the center of the star. The stellar radius R and luminosity L have to be computed to satisfy this boundary condition.

Having established the important physics governing a stationary star, the stellar structure can now be solved numerically. The most commonly used method for this is the Henyey method (Henyey *et al.* 1959; 1964). First, the functions are discretized along the radial direction. In practice, we parametrize space using the radial mass M_r (related to radius by the first equation of stellar structure) in order to follow the location of matter in the star[1]. The mass of the star is thus split up into around ∼1000 shells and the differential equations turn into difference equations. The solution of these is then approximated iteratively until a specific accuracy threshold has been surpassed.

The description so far only encompasses the solution of a stationary stellar model. We must now implement a time-dependent component that will drive the evolution of the star. For this, time is discretized into steps and after each step, various changes are first applied to the computed model, for example the change in chemical composition due to nuclear reactions, effects of diffusion and convection as well as mass loss. After these changes are applied, the Henyey algorithm will find the new state of hydrostatic equilibrium by adjusting R and L until the model converges in a solution of the stellar structure equations. In this fashion, the stellar model will evolve.

It is worth mentioning that GENEC's discretization of time and space is dynamic. The time step is adjusted automatically to be an optimal trade-off between total computation time, precision, and ease of convergence. This means that in stable phases such as the main sequence, one time step can represent ∼10 000 years of stellar evolution, whereas towards the end of central carbon burning, a time step can be as short as a few days. Interestingly, at some stage of the evolution model, the simulation becomes slower than real-time! Modeling until the end of central carbon burning requires on the order of 40 000 time steps. Similarly, GENEC also adjusts its definition of discrete shells with a type of algorithm known as adaptive mesh refinement (AMR). This automatically splits space into smaller intervals in regions containing a lot of detail such as high gradients and makes intervals broader where the star is more homogeneous.

2.2 Working with the stellar evolution code

Apart from the main code, GENEC includes some tools to aid the workflow of running a simulation, whose main steps I shall describe in the following.

First, we run a program that creates the initial model of the star. Here is where we give a name to the model and define the initial mass M_{ini}, metallicity $Z = 0.014$ (solar metallicity), and rotational speed $V = 0$. The program creates a so-called parameters file which contains all the initial parameters of the simulation including the entire stellar structure at the ZAMS. We are interested in studying different mass loss prescriptions in the RSG phase, which have been implemented in GENEC. At this point we can select the RSG mass loss prescription to follow by setting a parameter called `RSG_Mdot` in the parameters file. This mass loss regime will then be activated once the star enters the red supergiant phase.

[1] In fluid dynamics this is called Lagrangian parametrization.

The `RSG_Mdot` parameter can be set to 0, 1, or 2. These correspond to the following RSG mass loss prescriptions:

0: Old RSG mass loss prescription based on Crowther (2001), shown in Equation 1.3.
1: No specific mass loss for the RSG phase. Default mass loss by de Jager *et al.* (1988).
2: New RSG mass loss prescription by Beasor *et al.* (2020), shown in Equation 1.4.

I have included `RSG_Mdot` $= 1$ for the sake of completeness only as I will in fact focus exclusively on the other two prescriptions, comparing the results of the new prescription `RSG_Mdot` $= 2$ with the old one `RSG_Mdot` $= 0$.

We will again access the parameters file to modify convergence parameters in order to help the code find solutions in case of difficulty. I describe this in more detail in section 2.3.

Having set all the initial parameters, we use the GENEC launcher (written in Python) to launch a simulation. This is done from the command line, specifying the name of the model as well as some optional parameters. For example, since GENEC tracks the burning phases of the star, we can instruct the launcher to stop the computation automatically once the star reaches a specified burning phase, in this case neon ignition (phase 4) after the end of central carbon burning.

While running, the program produces some live output, allowing us to monitor the progress of the evolution. A screenshot of this can be seen in Figure 2.1.

```
##################################################       11205
Modele        11205
##################################################       11205
    age=   6807458.8539923122           m=          986
     Teff =  3.591889     L =  5.226855
TEFF ESTIMATION:    3.5918988890632861        5.2267378595087113
Modele converge
MAIN: vsuminenv=suminenv   1.3901485293714614E+060   1.4014727994967107E+060
##################################################       11206
Modele        11206
##################################################       11206
    age=   6807477.3719763299           m=          987
     Teff =  3.591812     L =  5.227029
TEFF ESTIMATION:    3.5918202721527965        5.2269682443515437
Modele converge
MAIN: vsuminenv=suminenv   1.4019122734774670E+060   1.4076146746060900E+060
##################################################       11207
Modele        11207
##################################################       11207
    age=   6807495.8899603477           m=          986
     Teff =  3.591742     L =  5.227199
TEFF ESTIMATION:    3.5917475058789030        5.2272436266885709
Modele converge
MAIN: vsuminenv=suminenv   1.4080366838424506E+060   1.4077887987529634E+060
```

Figure 2.1: Screenshot of GENEC output during runtime during the computation of the models for the timesteps 11205, 11206, 11207. It shows the age of the star at each step (in years), as well as the effective temperature and luminosity. This allows us to roughly monitor the evolution of the model and detect if the simulation is running too slowly.

If the program runs into no trouble, it computes the stellar evolution until the specified end point in around 6 hours[2], producing an assortment of data files along the way. One model stopped at the end of central carbon burning produces around 20 GB of data, which can conveniently be compressed to about 10% its size using a concatenation tool provided with GENEC. This tool extracts the time series of all the variables in the star, conjoins them into one array, which is then saved as a so-called evolution file. This file can then be read in Python using the utility GENEC_toolBox, from which point we can progress to data analysis and visualization.

[2] The computation time can be reduced by running the simulations on a supercomputer, however this is impractical if the code needs to be monitored at runtime and frequently paused, which turns out to be the case for these simulations.

2.3 Troubleshooting convergence difficulties

Unfortunately, a simulation running without interruption is the exception in this project. Since the Henyey method works by trying iteratively to converge towards a state of hydrostatic equilibrium, the code runs into difficulties if the model moves too far away from hydrostatic equilibrium after one time step. This is more common for more massive stars especially during the RSG phase, since these are hydrostatically less stable and are prone to heavy mass loss. When this causes the code to have trouble converging, it will first try to cut the time step in half in an attempt to move through the instability more slowly. If it still fails to converge, the code will keep halving the time step until a certain minimum limit is reached, at which point it will abort the computation.

When the program crashes, we have the possibility to edit certain convergence parameters manually in the parameters file. Although the program does try to adjust those parameters automatically throughout the simulation, human intervention is often ultimately necessary. There are various parameters that affect the convergence behavior of the code, which can be grouped into three categories.

Firstly, there are parameters that adjust the tolerance of a proposed solution to the stellar structure equations. Since these equations are continuous equations, they can never be solved exactly by a discrete algorithm. Therefore, a specific tolerance threshold must be defined, which we can loosen in case of convergence difficulty. This means that we are effectively accepting a less accurate model in order to continue the simulation.

Secondly, some parameters control the adaptive discretization of the model. The definition of a spatial and temporal step is based on a maximum difference in key variables such as pressure, density and luminosity from step to step. Decreasing this threshold leads to the code creating a finer discretization, which may converge more easily for the price of more computation time.

Thirdly, some parameters adjust the convergence speed, i.e. they decide how large of a correction is made after each iteration. The Henyey algorithm works with a linearized set of stellar structure equations and converges by gradient descent. The code scales the correction applied after each iteration by a factor which can be modified. Decreasing this factor makes the code converge more slowly but can avoid overshooting the solution.

Choosing which parameters to modify is based on trial and error as well as experience. When the program aborts, it does print some information indicating the source of the crash, but it is up to the operator to narrow this down to a specific physical or numerical cause.

Chapter 3

Results

The data analysis and extraction was done in Python and relied heavily on array computation module *numpy* (Harris *et al.* 2020). The plots were produced with the graphics module *matplotlib* (Hunter 2007). Some key results from this chapter are shown in Table A.1, in the Appendix.

3.1 Hertzsprung-Russell Diagrams

I present the computed stellar evolution tracks on the HRD with the old RSG mass loss prescription (RSG_Mdot=0) in Figure 3.1 and with the new RSG mass loss prescription (RSG_Mdot=2) in Figure 3.2. These figures also include photometric observations of RSGs done by Levesque *et al.* (2005). The end points of the tracks approximate the location of core collapse, since a star does not have time to move significantly in the HRD after the end of central carbon burning.

We see that the chosen RSG mass loss prescription has no effect on the qualitative evolution of stars with an initial mass of up to 20 $M_\odot$. For both prescriptions, the stellar surface cools as helium burning begins and the star quickly approaches the RSG phase. The 12 $M_\odot$ model performs a blue loop during central helium burning, an effect that can be attributed to downward convective overshooting in the stellar envelope (Wagle *et al.* 2019). Apart from the blue loop, the stars stay in the RSG phase until their death.

The path of evolution after reaching the RSG phase splits significantly depending on the chosen RSG mass loss prescription for initial masses above 20 $M_\odot$. While for RSG_Mdot=2 the evolution is qualitatively similar to that of lower mass stars, for RSG_Mdot=0 the stars eventually leave the RSG phase and become yellow or blue supergiants (YSG/BSG). This is due to this mass loss prescription causing significantly heavier mass loss, stripping away a significant fraction of the hydrogen envelope and exposing the hotter inner layers of the star. This fact will be clarified when we compare the mass loss directly (section 3.2) as well as the surface abundances (section 3.5) resulting from the two RSG mass loss prescriptions.

Considering the observations by Levesque *et al.* (2005), we notice fairly homogeneous distribution of RSGs across luminosities ranging from $\log(L/L_\odot) \approx 4.0$ to $\log(L/L_\odot) \approx 5.5$. Figure 3.2 shows that with RSG_Mdot=2 the models can produce RSGs in this entire range. Figure 3.1 indicates that by applying the old mass loss prescription (RSG_Mdot=0), RSGs above $\log(L/L_\odot) \gtrsim 5.25$ tend to depart from the RSG phase, making observations in this domain less likely. This can be better quantified by comparing the time spent in the RSG phase, which I develop in section 3.3.

Ultimately, the old mass loss prescription causes the most massive stars in the considered range to die as BSGs or YSGs, as was the case in the supernova SN1987A (Arnett *et al.* 1989).

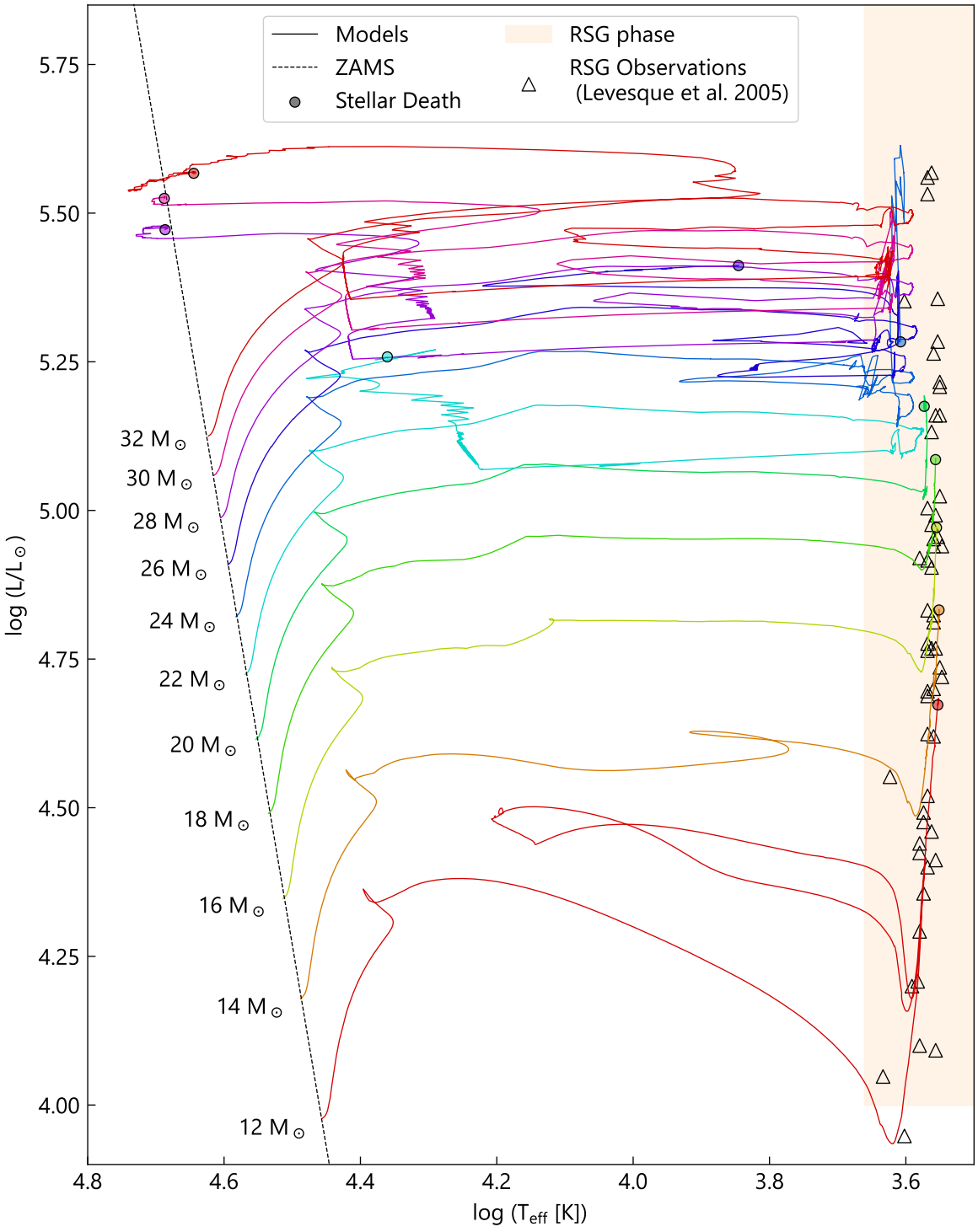

Figure 3.1: Hertzsprung-Russell diagram showing the evolution of 11 stellar models of initial masses ranging from 12 $M_\odot$ to 32$_\odot$, with solar metallicity ($Z = 0.014$), no rotation, and using the old RSG mass loss prescription (RSG_Mdot = 0) in Equation 1.3, based on Crowther (2001). The theoretical zero-age main sequence is represented by a power law shown as a black dashed line. The colored circles show the location of the star at death and the black triangles are photometric observations of Galactic RSGs presented in Levesque *et al.* (2005).

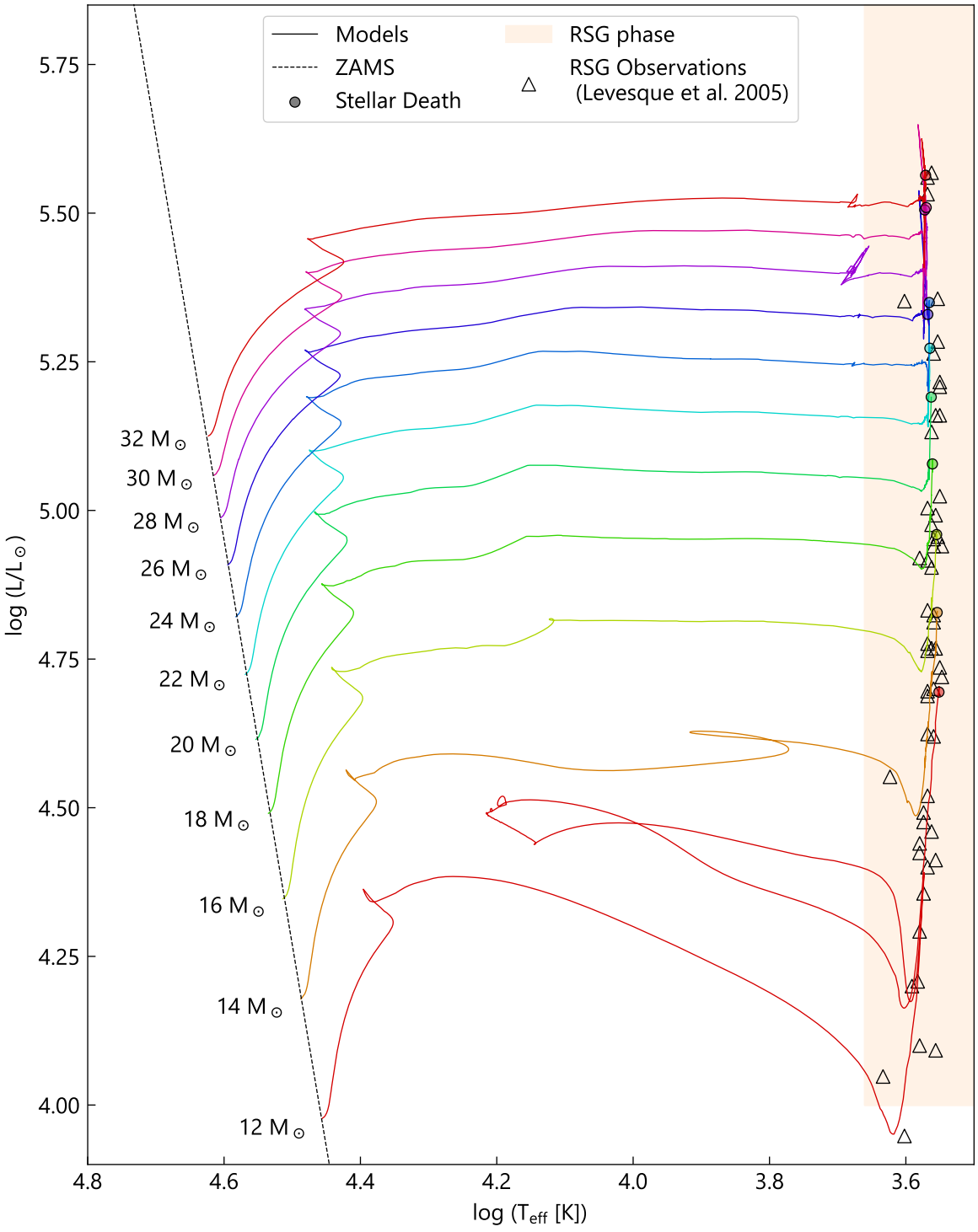

Figure 3.2: Hertzsprung-Russell diagram showing the evolution of 11 stellar models of initial masses ranging from 12 $M_\odot$ to 32$_\odot$, with solar metallicity ($Z = 0.014$), no rotation, and using the new RSG mass loss prescription (RSG_Mdot = 2) in Equation 1.4, based on Beasor *et al.* (2020). The theoretical zero-age main sequence is represented by a power law shown as a black dashed line. The colored circles show the location of the star at death and the black triangles are photometric observations of Galactic RSGs presented in Levesque *et al.* (2005).

3.2 Mass loss

Figure 3.3 shows the total mass loss over the course of the stellar lifetime for both RSG mass loss prescriptions. This also includes mass lost outside of the RSG phase, which is governed by different prescriptions not discussed in this study. The final mass at death follows directly from this and is shown in Figure 3.4. We learn that the new mass loss prescription (RSG_Mdot=2) leads to considerably lesser mass loss than the old prescription.

In Figure 3.5 we see the mass lost in the RSG phase. This was obtained by summing the mass lost over all time steps where the star was flagged as 'RSG'. The y axis is in logscale in order to facilitate comparison of both mass loss prescriptions, since the resulting mass loss differs by 1∼2 orders of magnitude. In addition to the simulation results, we show an estimate by Beasor & Davies (2018) from observations which later formed the basis of their proposed prescription that is the subject of this study. Curiously, the model for 16 $M_\odot$ resulting from their prescription loses approximately ten times less mass in the RSG phase than they estimated. This discrepancy is in part due to their overestimating the time a star spends in the RSG phase compared to results from GENEC, but given the order of magnitude of the devitation, other causes are to be expected.

An noteworthy artefact of the results in Figure 3.5 is the sharp increase in mass loss at 20 $M_\odot$ for both prescriptions. This is due to an artificial enhancement of the mass loss rate by a factor 3 that is applied by GENEC when the star's luminosity exceeds its Eddington luminosity[1] by more than a factor 5 (Ekström *et al.* 2012), which happens for giant stars of initial mass $\gtrsim$19 $M_\odot$. In the supra-Eddington regime, heavy mass loss is expected due to dominating radiation pressure, which is the motivation for this enhancement. Its implementation is also necessary for numerical reasons, since GENEC searches for a hydrostatic equilibrium state, which is difficult to find in a supra-Eddington star without supplementary mass loss. The effect of the mass loss rate multiplier is visible also looking at the total mass loss (Figure 3.3) and final mass (Figure 3.4) for the old RSG mass loss prescription (RSG_Mdot=0), whose already high base rate is significantly amplified.

3.3 Timescales

Given qualitative stellar evolution theory summarized in section 1.2, we know that a massive star will spend on the order of 1 Myr in its post-MS life, most of this in the RSG phase. In this section, I analyze the total time τ_{RSG} that a star spends RSG phase, which I will call the RSG timescale. This quantity is directly related to the probability of observing a star in the RSG phase, which provides an important anchor point to test stellar models against observations.

The RSG timescale depends strongly on whether a star departs again from the RSG phase after reaching it, as well as on the overall speed of evolution which is correlated with inital mass. Figure 3.6 shows the RSG timescale of the models as a function of initial mass. For both RSG mass loss prescriptions, we see a decreasing trend in τ_{RSG} with increasing initial mass, ignoring the outlier at 12 $M_\odot$ which has a considerably shorter RSG timescale due to the presence of a blue loop (see Figure 3.1 and Figure 3.2). Up to an initial mass of 24 $M_\odot$, the RSG timescale is fairly similar for both mass loss prescriptions. At higher initial masses, the models bifurcate, with the RSG timescale leveling off for RSG_Mdot=2 while continuing on its descent for RSG_Mdot=0. For the highest initial mass models considered, the new mass loss prescription causes the star to remain about three times as long in the RSG phase because of its absence of late-stage blueward evolution.

Another interesting quantity to consider is the ratio of the RSG timescale and the BSG timescale. This can be used to predict the ratio of RSGs to BSGs among stellar populations, which is an observational test for stellar evolution models. The RSG-BSG ratio was discussed for example by Eggenberger *et al.* (2002) in an observational study for different metallicities and more recently by Wagle *et al.* (2020) in the Large Magellanic Cloud.

[1] The Eddington luminosity is the luminosity at which radiation pressure balances gravity. It can be seen as a theoretical upper limit of the luminosity of a star in hydrostatic equilibrium.

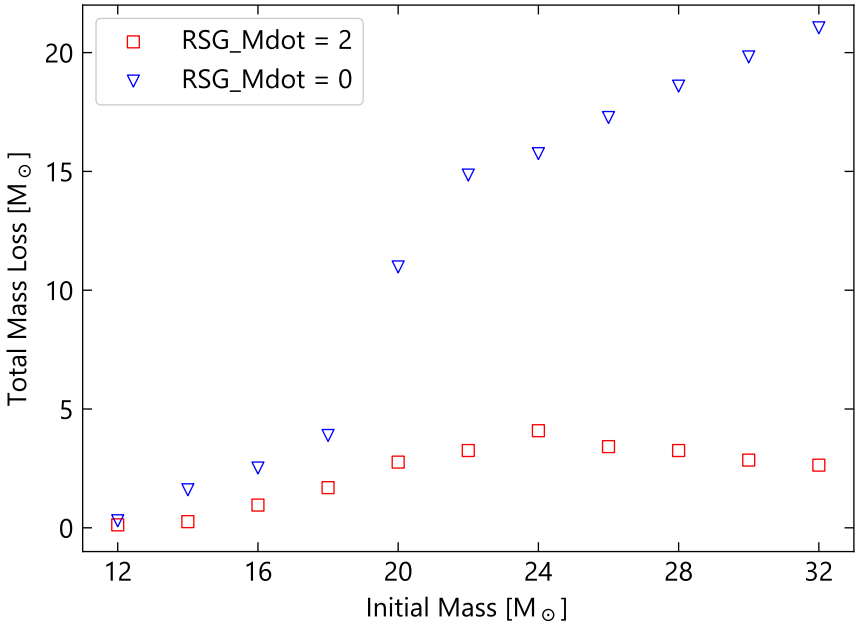

Figure 3.3: Total mass loss in the life of the stellar models for both RSG mass loss prescriptions.

.

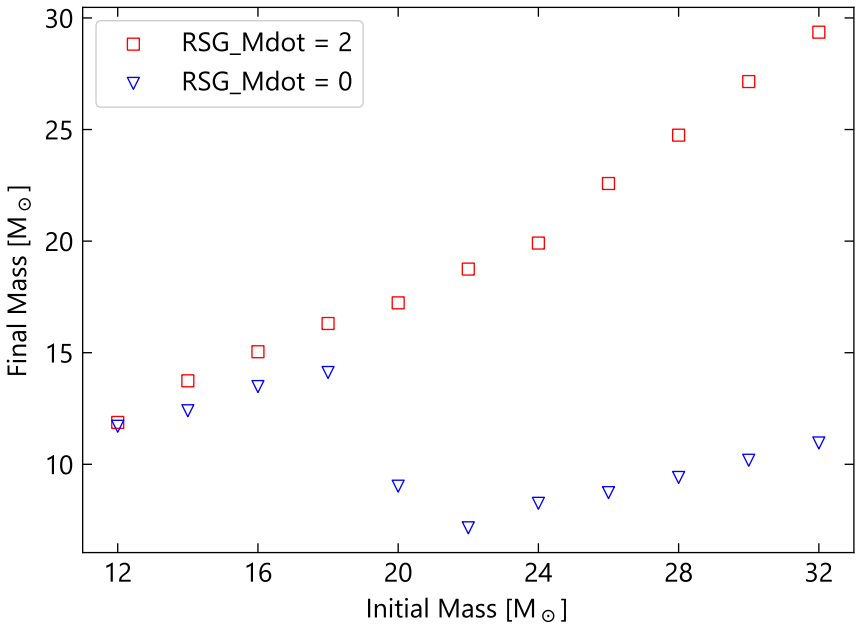

Figure 3.4: Final mass of the stellar models for both RSG mass loss prescriptions.

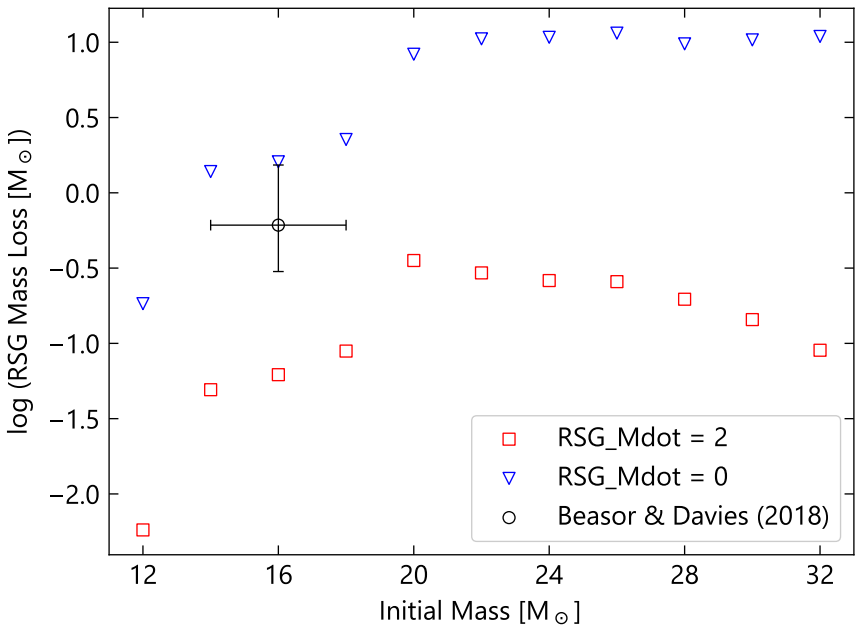

Figure 3.5: Mass loss integrated over the RSG phase of the stellar models for both RSG mass loss prescriptions. An estimate of the mass lost by a 16 $M_{\odot}$ star during the RSG phase based on Galactic cluster observations is shown (Beasor & Davies 2018).

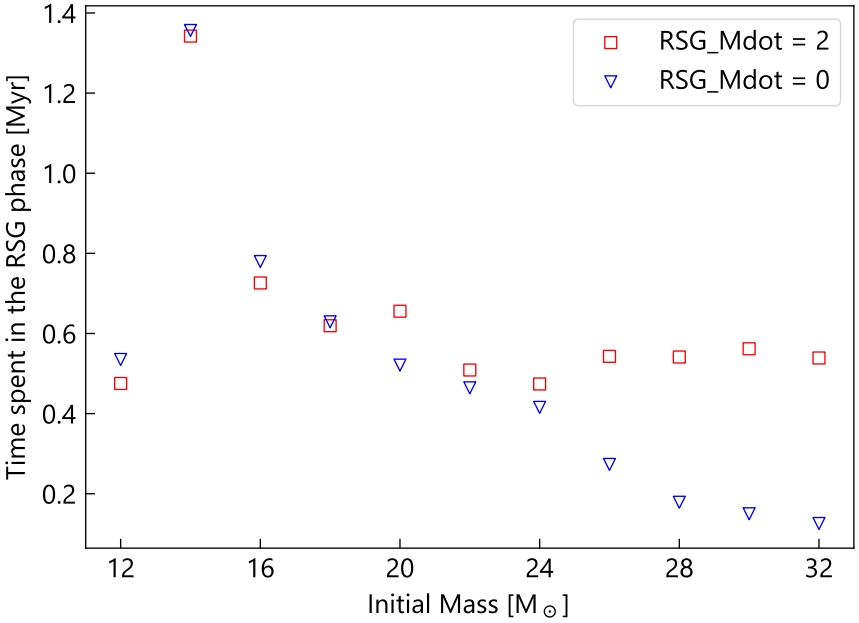

Figure 3.6: Time spent in the RSG phase by the stellar models for both RSG mass loss prescriptions.

I present the RSG-BSG timescale ratio obtained from the simulations in Figure 3.7. Up to an initial mass of 24 $M_\odot$, the ratio is almost independent of the applied RSG mass loss prescription. Above this mass, we see that the new mass loss prescription (RSG_Mdot=2) considerably favors the red over the blue supergiant, which is not the the case for the old mass loss prescription. At an initial mass of at least 28 $M_\odot$, the RSG-BSG timescale ratio drops below unity using the old mass loss prescription, indicating that BSGs should be prevalent over RSGs in this mass range, should that prescription be accurate.

The large disparity of RSG-BSG timescale ratios between the two mass loss prescriptions at high initial masses should make it easy to conclusively compare their validity observationally. To take the extreme example, in a population of stars of 32 $M_\odot$ initial mass, the new mass loss prescription predicts an abundance of RSGs vs BSGs that is 30 times higher than is predicted by the old mass loss prescription.

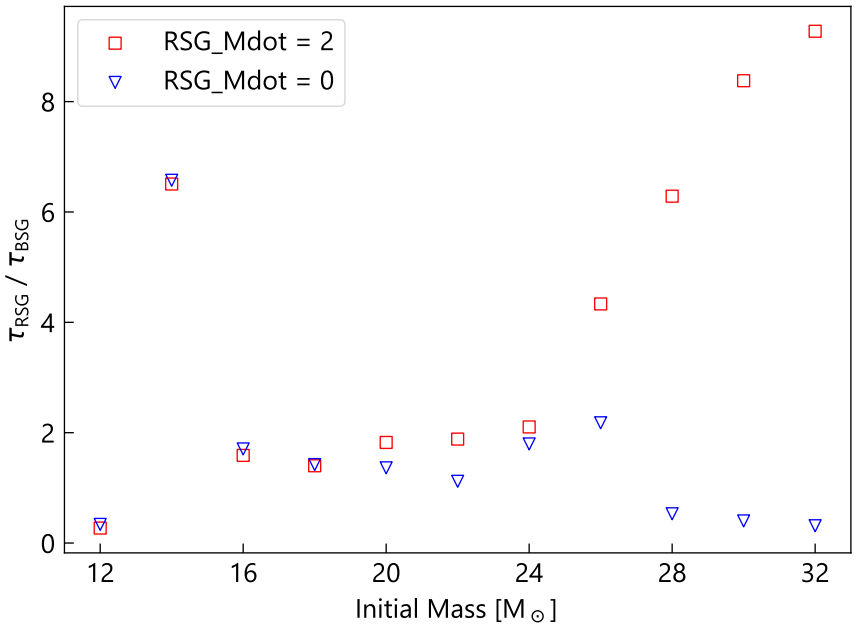

Figure 3.7: Ratio of the time spent in the RSG phase vs. the BSG phase by the stellar models for both RSG mass loss prescriptions.

3.4 A mass-luminosity relation for red supergiants

Mass-luminosity relations are often helpful to connect the difficult-to-observe quantity of mass with the directly observable luminosity. The simulated mass-luminosity relation for RSGs is shown in Figure 3.8. In order to establish this relation, I time-averaged the mass and luminosity data of the models during the RSG phase and used the standard deviations of these quantities as error bars. The latter is important in order to account for heavy mass loss experienced during the RSG phase with the old RSG mass loss prescription. Looking at the graph, we notice no clearly discernible relationship with the old mass loss prescription, while the new prescription results in a clearly confined trend. It may be worth noting that the new prescription also produces slightly less luminous RSGs.

We can also compare the time-averaged RSG luminosity to the initial mass, as is shown in Figure 3.9. The resulting trend is more linear than in Figure 3.8, which in double logarithmic scaling is a power law. I fitted the data for RSG_Mdot=2 with a powerlaw of the form $L_{\mathrm{RSG}} = bM_{\mathrm{ini}}^{a}$, whose optimal parameters were determined as $a = 2.47 \pm 0.09$ and $b = 66 \pm 19$.

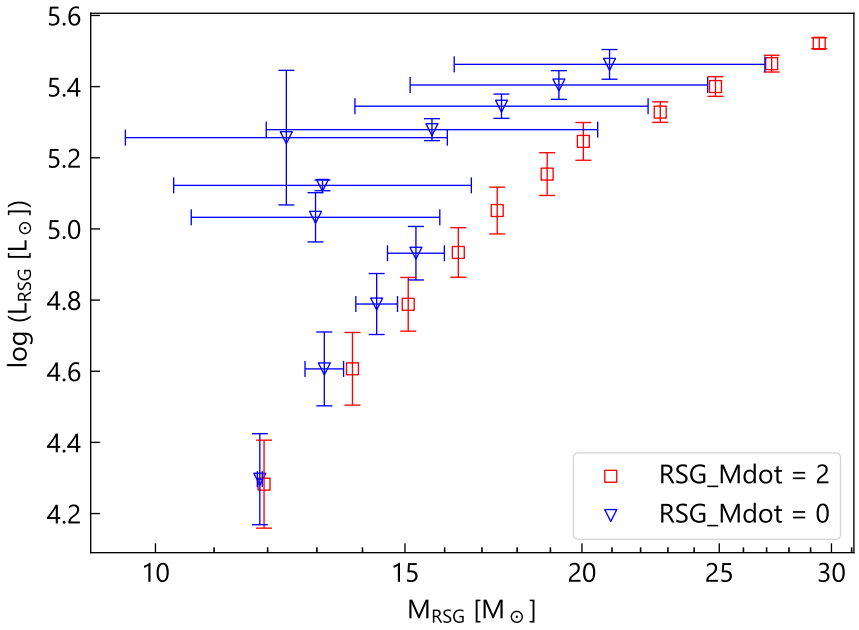

Figure 3.8: The mass-luminosity relation for model RSGs.

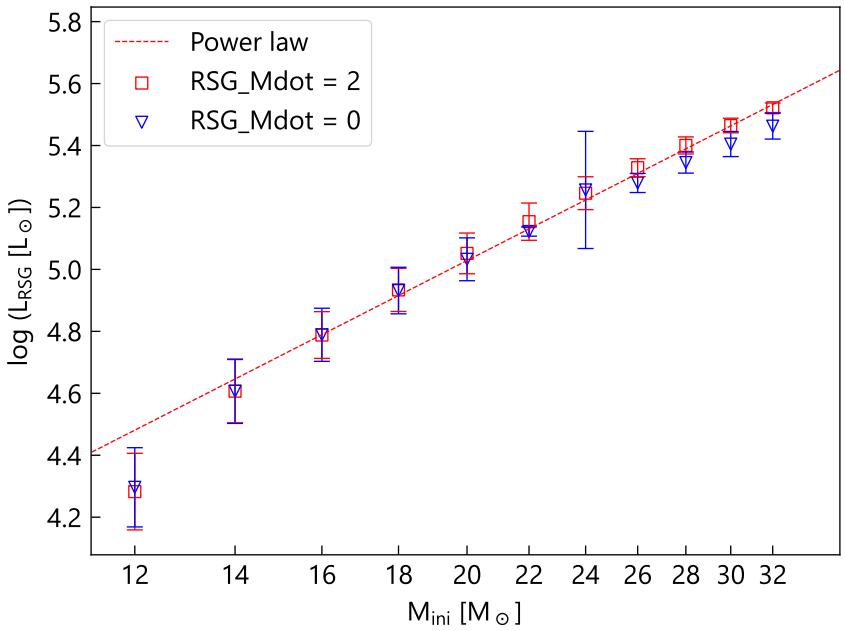

Figure 3.9: The initial mass-luminosity relation for model RSGs. The data for the new mass loss prescription (RSG_Mdot=2) was fit by a power law shown as a dashed red line.

3.5 Evolution of chemical surface abundances

Finally, let us consider the evolution of the mass fraction of various chemical species on the stellar surface. Surface abundances are a prediction made by stellar evolution models that can be observed spectroscopically, as was done for example for supernova progenitors such as RSGs by Boian & Groh (2020). Here I present the simulated evolution of surface abundances of hydrogen, helium, and carbon in Figure 3.10. The abundances represent the sum over all present isotopes of each element.

Initially, the star is fully mixed with the chemical abundances fixed by the initial model. At solar metallicity, the initial mass fractions used by the GENEC model were calibrated to reproduce the observed radius, luminosity, and surface abundances of the present-day sun, taking into account stellar evolution until solar age including atomic diffusion (Ekström *et al.* 2012).

$$\mathrm{H} : 72.0\% \qquad \mathrm{He} : 26.6\% \qquad \mathrm{C} : 0.2311\% \tag{3.1}$$

The initial abundances remain unchanged on the surface throughout the main sequence and are only affected once the star starts expanding after central helium ignition. This happens earlier the more massive a star is initially. The large temperature gradient that is established between the stellar interior and the surface causes the envelope to become convective, dredging up products of interior nuclear reactions to the surface. Mixing in the envelope thus means that the surface abundances will tend to equalize with the abundances in interior layers during the post-MS evolution.

We see that surface hydrogen abundance drops, to be replaced with helium from the interior. Additionally, the surface carbon abundance decreases after the main sequence. This is a consequence of carbon being a catalyst of a hydrogen-fusion process known as a CNO cycle, which is the dominant fusion process in massive stars (See Ekström 2021). Thus, carbon will be depleted in the center during nuclear burning in the main sequence, which manifests itself on the surface after dredge-up.

The results also show that the changes in surface abundances are more extreme with the old RSG mass loss prescription (RSG_Mdot=0) than with the new prescription (RSG_Mdot=2). This is a result of heavier mass loss which exposes a deeper layer of the star to the surface. In the extreme case, for the 32 $M_\odot$ star modeled with the old prescription, almost no hydrogen envelope remains by the star reaches the end of central carbon burning.

It must be noted that, contrary to the endpoints on the HRD, the endpoints of the tracks in Figure 3.10 do not accurately represent the state of the models at core collapse. While HRD position or mass loss cannot significantly change in the remaining few years after the end of the simulation, the surface abundances evolve on the convection timescale, which can be as short as a few weeks near the surface (Kravchenko *et al.* 2019). There is therefore the possibility of witnessing considerable change in surface abundances during the post-central-carbon-burning stages of evolution, which were not captured by these models.

As a final point, it may be interesting to note that the final surface hydrogen abundance for RSG_Mdot=2 seems to decrease with increasing initial mass across the entire mass range, although the total mass loss peaks at $M_{\mathrm{ini}} = 24\ M_\odot$ (Figure 3.3). This suggests that the loss of the hydrogen envelope is not the only factor driving the change in surface abundances.

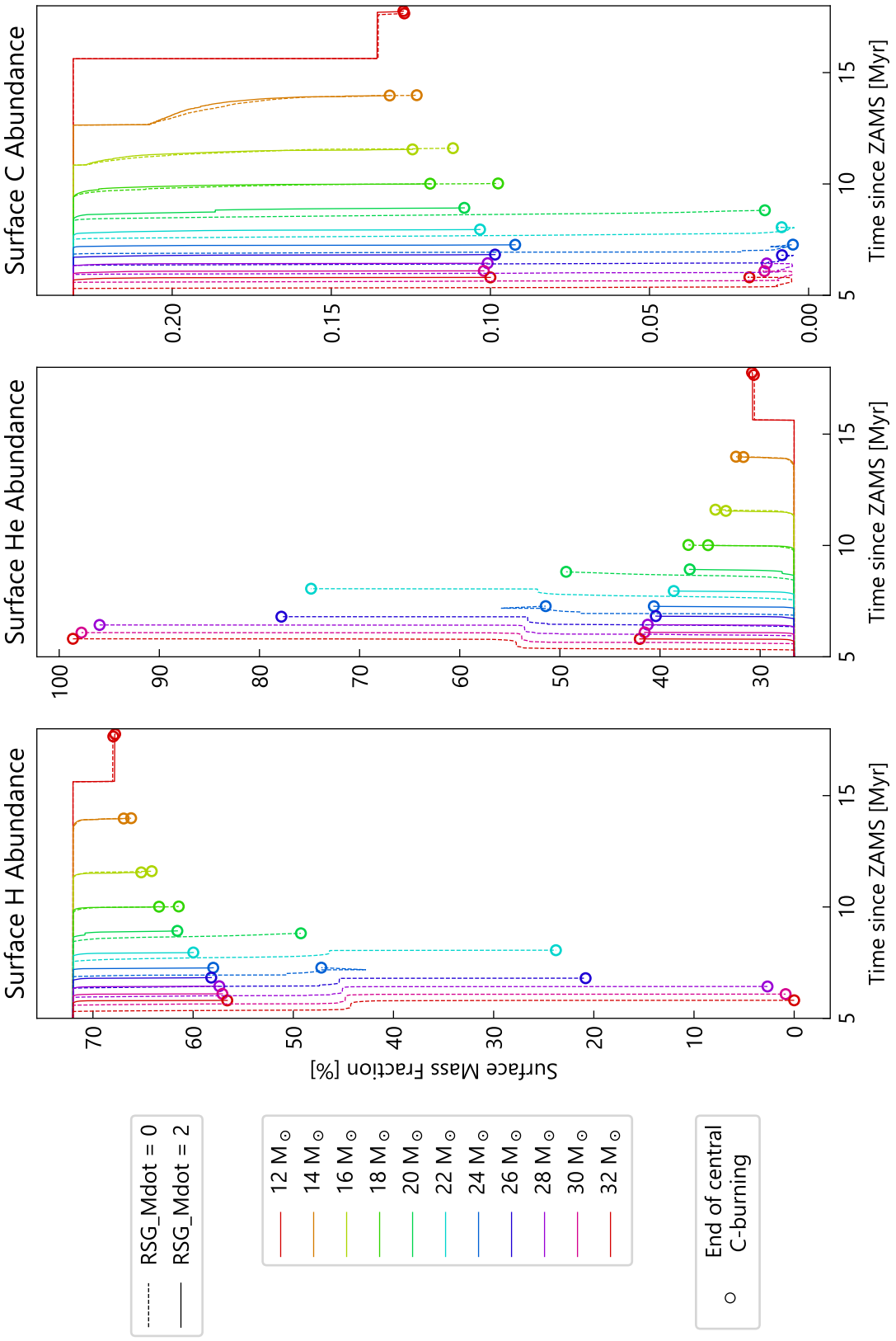

Figure 3.10: Evolution of surface abundances of hydrogen, helium and carbon for stellar models until the end of central carbon burning.

Chapter 4

Discussion and conclusion

In this work I computed non-rotating stellar models of solar metallicity using the new RSG mass loss prescription proposed by Beasor *et al.* (2020), as well as models using the old prescription based on Crowther (2001) for comparison. The results clearly show that the new prescription leads to a much lower mass loss rate in the RSG phase (even much lower than estimates by Beasor & Davies (2018) suggest). This is consistent with models using the new prescription computed using the MESA evolution code by Beasor *et al.* (2021). The lower mass loss rate prevents the models from evolving back to the blue as is the case using the old prescription with stars of above 20 $M_\odot$ initial mass. As a consequence, the new mass loss rate predicts a much higher RSG-BSG ratio in the higher-mass range, which could be observable in population studies. T

It is worth discussing the apparent incongruence between these results and the lack of observations of RSG supernova progenitors at initial masses above 20 $M_\odot$ (Li *et al.* 2007), known as the "red supergiant problem". The idea is that, given that most massive stars end their evolution as red supergiants according to some models (such as the one presented here), then why haven't we found any red supergiants above a luminosity of $\log(L/L_\odot) \gtrsim 5.2$ in supernova progenitor studies?[1] The review by Smartt (2009) discussed possible resolutions of this tension, one of which is the possibility of mass loss causing RSGs to evolve back to the blue and explode as blue supergiants. However, there is reason to believe that current models tend to overestimate mass loss in RSGs (Beasor & Davies 2016; 2018), giving more weight to alternative explanations of the RSG problem. Smartt (2015) finds that massive RSGs could possibly die 'silently' by direct collapse into black holes with no, or only very faint, explosions. The advantage of this theory is its ability to explain the lack of RSG supernova progenitors of high luminosities, while still agreeing with direct observations of luminous RSGs, for example those by Levesque *et al.* (2005) shown in Figure 3.2. In another approach analyzing the statistical significance of the RSG problem, it can also be shown that given limited observational sample size, the tension between the maximum observed luminosity of RSG supernova progenitors and its expected upper limit is within 2σ and hence not (yet) significant enough to cause concern (Davies & Beasor 2018; 2020).

In this work, I also studied the evolution of the surface abundances of light elements, which could constitute a way of testing the simulations against observations. The results showed that the new RSG mass loss prescription results in less dredge-up of nuclear fusion products from the core, and that this dredge-up increases with increasing initial mass.

The logical continuation of this study would be to interpolate key results from the computed stellar evolution grid and apply it to a stellar population to obtain expected distributions of various parameters related to RSGs. Correcting for observational bias, these population syntheses are direct predictions that can be validated or invalidated observationally.

It must, however, be noted that predictability is constrained by the scope of parameters considered in this study, specifically regarding rotation and metallicity. Both of these parameters are known to have significant effects on different aspects of stellar evolution, in-

[1] The maximum luminosity of RSG supernova progenitors is the observable quantity that can be linked to a maximum initial mass with stellar evolution models. (See section 3.4)

cluding mass loss. For example, it is not hard to imagine that a high rotation rate will favor mass loss near the equator. The effect of metallicity may be less obvious, but it is known that the observed RSG-BSG ratio is in fact very sensitive to the regional metallicity (Eggenberger *et al.* 2002), suggesting that accurate stellar evolution models should include a metallicity-dependent component in the RSG mass loss prescription. Beasor *et al.* (2020) argued that the observed correlation between RSG mass loss rate and luminosity at similar initial mass was tight even without constraining the sample to a single metallicity, prompting them to exclude metallicity as a parameter in their proposed RSG mass loss prescription (Equation 1.4), using only luminosity and initial mass instead.

One may argue that initial mass cannot be a logical component of any prescription used in late-stage stellar evolution since it is not a directly observable quantity. The initial mass of a star can only be inferred using evolution models on the assumption that the star has followed a classical single-star evolution for its whole life. This procedure not only includes all the errors of the model (which can be significant for a star in late-phase evolution), but also completely disregards the possibility of stars having a history of binary evolution and mergers, which can completely change the evolution of a star. Since 70% of massive stars will have a mass-exchanging interaction with a binary companion at some point in their lifetimes (Sana *et al.* 2012), the influence of this phenomenon on the properties of red supergiants cannot be negligible.

To conclude, mass loss is an important factor driving the late stage evolution of massive stars and will ultimately determine the life of a red supergiant and its possibility of becoming a supernova progenitor. Stellar evolution codes treat mass loss using empirical prescriptions, which are based on observational calibration rather than fundamental physics. It is therefore an ongoing endeavor to find robust tests of different prescriptions by considering a wide parameter space both in modeling and observational surveys. Finally, more precise mass loss prescriptions using more variables and operating on shorter timescales could also be expored.

Acknowledgements

Sylvia, I would like to express to you my fullest gratitude for your excellent guidance throughout this project. Your availability, investment and commitment to helping, supporting, and discussing with me were invaluable contributors to my progress this semester. I very much look forward to continuing working with you for my M.Sc. thesis project next year!

References

(1) Arnett, W. D. *et al.* Supernova 1987A. *ARA&A* **27,** 629–700 (1989).

(2) Beasor, E. R. & Davies, B. The evolution of red supergiants to supernova in NGC 2100. *MNRAS* **463,** 1269–1283 (2016).

(3) Beasor, E. R. & Davies, B. The evolution of red supergiant mass-loss rates. *MNRAS* **475,** 55–62 (2018).

(4) Beasor, E. R. *et al.* A new mass-loss rate prescription for red supergiants. *MNRAS* **492,** 5994–6006 (2020).

(5) Beasor, E. R. *et al.* The Impact of Realistic Red Supergiant Mass Loss on Stellar Evolution. *ApJ* **922,** 55 (2021).

(6) Boian, I. & Groh, J. H. Progenitors of early-time interacting supernovae. *MNRAS* **496,** 1325–1342 (2020).

(7) Crowther, P. A. *Stellar Winds from Massive Stars* in *The Influence of Binaries on Stellar Population Studies* (ed Vanbeveren, D.) **264** (2001), 215.

(8) Davies, B. & Beasor, E. R. The initial masses of the red supergiant progenitors to Type II supernovae. *MNRAS* **474,** 2116–2128 (2018).

(9) Davies, B. & Beasor, E. R. The 'red supergiant problem': the upper luminosity boundary of Type II supernova progenitors. *MNRAS* **493,** 468–476 (2020).

(10) De Jager, C. *et al.* Mass loss rates in the Hertzsprung-Russell diagram. *A&AS* **72,** 259–289 (1988).

(11) Eggenberger, P. *et al.* The blue to red supergiant ratio in young clusters at various metallicities. *A&A* **386,** 576–582 (2002).

(12) Eggenberger, P. *et al.* The Geneva stellar evolution code. *Ap&SS* **316,** 43–54 (2008).

(13) Ekström, S. *et al.* Grids of stellar models with rotation. I. Models from 0.8 to 120 $M_{\odot}$ at solar metallicity (Z = 0.014). *A&A* **537,** A146 (2012).

(14) Ekström, S. Massive star modelling and nucleosynthesis. *Frontiers in Astronomy and Space Sciences* **8,** 53 (2021).

(15) Harris, C. R. *et al.* Array programming with NumPy. *Nature* **585,** 357–362 (2020).

(16) Henyey, L. G. *et al.* A Method for Automatic Computation of Stellar Evolution. *ApJ* **129,** 628 (1959).

(17) Henyey, L. G. *et al.* A New Method of Automatic Computation of Stellar Evolution. *ApJ* **139,** 306 (1964).

(18) Hunter, J. D. Matplotlib: A 2D graphics environment. *Computing in Science & Engineering* **9,** 90–95 (2007).

(19) Kravchenko, K. *et al.* Tomography of cool giant and supergiant star atmospheres. II. Signature of convection in the atmosphere of the red supergiant star μ Cep. *A&A* **632,** A28 (2019).

(20) Levesque, E. M. *et al.* The Effective Temperature Scale of Galactic Red Supergiants: Cool, but Not As Cool As We Thought. *ApJ* **628,** 973–985 (2005).

(21) Li, W. *et al.* On the Progenitors of Two Type II-P Supernovae in the Virgo Cluster. *ApJ* **661,** 1013–1024 (2007).

(22) Maeder, A. *Physics, Formation and Evolution of Rotating Stars* (Springer Berlin, Heidelberg, 2009).

(23) Neugent, K. F. *et al.* The Luminosity Function of Red Supergiants in M31. *ApJ* **889,** 44 (2020).

(24) Rouan, D. in *Encyclopedia of Astrobiology* (eds Gargaud, M. *et al.*) 479–480 (Springer Berlin, Heidelberg, 2011).

(25) Sana, H. *et al.* Binary Interaction Dominates the Evolution of Massive Stars. *Science* **337,** 444 (2012).

(26) Smartt, S. J. Observational Constraints on the Progenitors of Core-Collapse Supernovae: The Case for Missing High-Mass Stars. *PASA* **32,** e016 (2015).

(27) Smartt, S. J. Progenitors of Core-Collapse Supernovae. *ARA&A* **47,** 63–106 (2009).

(28) Sylvester, R. J. *et al.* Silicate and hydrocarbon emission from Galactic M supergiants. *MNRAS* **301,** 1083–1094 (1998).

(29) Van Loon, J. T. *et al.* Mass-loss rates and luminosity functions of dust-enshrouded AGB stars and red supergiants in the LMC. *A&A* **351,** 559–572 (1999).

(30) Wagle, G. A. *et al.* Type IIP Supernova Progenitors and Their Explodability. I. Convective Overshoot, Blue Loops, and Surface Composition. *ApJ* **886,** 27 (2019).

(31) Wagle, G. A. *et al.* Type IIP Supernova Progenitors. III. Blue to Red Supergiant Ratio in Low-metallicity Models with Convective Overshoot. *ApJ* **894,** 118 (2020).

Appendix A

Data Table

$M_{\rm ini}$ $[M_\odot]$	RSG_ Mdot	$M_{\rm final}$ $[M_\odot]$	$\Delta M_{\rm tot}$ $[M_\odot]$	$\Delta M_{\rm RSG}$ $[M_\odot]$	$\tau_{\rm RSG}$ $[10^5$ yr]	$\log(\overline{L_{\rm RSG}}/L_\odot)$	$\sigma(\log(\overline{L_{\rm RSG}}/L_\odot))$
12	0	11.70	0.30	0.18	5.35	4.30	0.13
	2	11.88	0.12	0.006	4.75	4.28	0.12
14	0	12.40	1.60	1.38	13.56	4.61	0.10
	2	13.74	0.26	0.05	13.42	4.61	0.10
16	0	13.48	2.52	1.61	7.80	4.79	0.09
	2	15.04	0.96	0.06	7.26	4.80	0.08
18	0	14.11	3.89	2.26	6.29	4.93	0.08
	2	16.31	1.69	0.09	6.19	4.93	0.07
20	0	9.02	10.98	8.33	5.21	5.03	0.07
	2	17.23	2.77	0.36	6.56	5.05	0.07
22	0	7.15	14.85	10.54	4.64	5.12	0.01
	2	18.75	3.25	0.29	5.09	5.15	0.06
24	0	8.25	15.75	10.79	4.15	5.26	0.19
	2	19.91	4.09	0.26	4.74	5.25	0.05
26	0	8.73	17.27	11.50	2.73	5.28	0.03
	2	22.58	3.42	0.26	5.43	5.33	0.03
28	0	9.41	18.59	9.76	1.79	5.34	0.03
	2	24.75	3.25	0.20	5.41	5.40	0.03
30	0	10.18	19.82	10.37	1.50	5.40	0.04
	2	27.15	2.85	0.14	5.62	5.44	0.02
32	0	10.96	21.04	10.93	1.26	5.46	0.04
	2	29.36	2.64	0.09	5.39	5.52	0.02

Table A.1: Data extracted from the GENEC models showing characteristic results, from left to right: the initial mass, the RSG mass loss prescription, the final mass at death, the total mass loss, the mass loss during the RSG phase, the time spent in the RSG phase, and the time-averaged luminosity in the RSG phase with its error.